



Universiteit
Leiden
The Netherlands

Integrating AFM into an STM and Creating a Tip-Enhanced Raman Spectroscopy Setup

Wit, Bob de

Citation

Wit, B. de. (2024). *Integrating AFM into an STM and Creating a Tip-Enhanced Raman Spectroscopy Setup*.

Version: Not Applicable (or Unknown)

License: [License to inclusion and publication of a Bachelor or Master Thesis, 2023](#)

Downloaded from: <https://hdl.handle.net/1887/3731882>

Note: To cite this publication please use the final published version (if applicable).



Integrating AFM into an STM and Creating a Tip-Enhanced Raman Spectroscopy Setup

THESIS

submitted in partial fulfillment of the
requirements for the degree of

MASTER OF SCIENCE

in

PHYSICS

Author :	B.C de Wit
Student ID :	s2005409
Supervisor :	Prof. dr. J.M. van Ruitenbeek
2 nd corrector :	Dr. M.J.A. de Dood

Leiden, The Netherlands, March 5, 2024

Integrating AFM into an STM and Creating a Tip-Enhanced Raman Spectroscopy Setup

B.C de Wit

Huygens-Kamerlingh Onnes Laboratory, Leiden University
P.O. Box 9500, 2300 RA Leiden, The Netherlands

March 5, 2024

Abstract

STM and AFM are two microscopic techniques used since the 1980s to discover the properties of materials and open a new world of material science. A significant drawback is the lack of chemical information that those microscope techniques give. To combat this problem in the van Ruitenbeek lab, we have set out to create a Scanning Tip Enhanced Raman Spectroscopy setup with simultaneous STM or AFM capabilities. This will allow us to simultaneously extract chemical information at a molecular resolution and obtain topographic data. This thesis discusses our challenges while adding AFM capabilities to an STM setup. Together with the integration of this new setup with a Raman spectroscope. And the measurements that are taken with these setups.

Contents

1	Theoretical Background and Methods	7
1.1	The Goal	7
1.2	Scanning Tunneling Microscopy(STM)	8
1.2.1	Tunneling Current	8
1.2.2	Application to STM	10
1.3	Atomic Force Microscopy(AFM)	11
1.3.1	The Lennard Jones Potential	11
1.3.2	The AFM Operation principle	14
1.4	Raman Spectroscopy	18
1.4.1	The diatomic molecule	18
1.4.2	Tip-enhanced Raman Spectroscopy	20
1.4.3	Comparing Raman Spectroscopy and Infrared spectroscopy	24
2	Instrumentation and Fabrication Methods	25
2.1	STM Instrumentation	25
2.2	AFM Instrumentation	26
2.3	Raman Spectroscopy	28
2.4	Fabrication of STM and AFM tips	28
2.4.1	Sample Fabrication	29
3	Results and Discussion	31
3.1	STM Measurements on gold	31
3.2	Combining AFM and STM	32
3.2.1	What type of AFM measurements?	32
3.2.2	Cantilever or Tuning Fork?	33
3.2.3	Fabrication of the Tuning Fork AFM tip	34
3.3	AFM Measurements	36
		5

3.4	Combining AFM and STM setups	38
3.4.1	Tunneling Current	38
3.5	Combined AFM/STM Measurements	39
3.6	Combining STM/AFM with Raman Spectroscopy	42
3.6.1	Geometry	42
3.6.2	STM/AFM tip holder	42
3.7	Raman Spectroscopy Results	44
3.8	STM on HOPG under the Raman Microscope	45
4	Outlook	49

Theoretical Background and Methods

To understand the design choices we made when adding Atomic Force Microscopy (AFM) functionality to our Scanning Tunneling Microscope (STM), we will need to know why we want our STM with AFM capabilities and the theoretical background of both STM and AFM. Furthermore, adding AFM capabilities is not the only goal. The end goal is Tip-Enhanced Raman Spectroscopy (TERS) with simultaneous AFM/STM. Thus, after discussing the theory behind AFM and STM, we will discuss the theory behind Raman spectroscopy and TERS.

1.1 The Goal

In the Van Ruitenbeek Lab, we already have STM and Raman Spectroscopy capabilities. And an interest in looking at graphene edges after chemical modification. But these are separate setups and correlated topographic and electronic data are required to characterize graphene edges after chemical modification. Thus we have set out to combine Raman Spectroscopy and STM.

However, measuring graphene with STM is not ideal, and AFM would be preferred to obtain topographic data. However, because STM gives information about the electronic structure, the ability to measure STM simultaneously would be beneficial. This is why we plan to extend our system with AFM capabilities.

This leaves the chemical data. The idea is to use Raman Spectroscopy simultaneously with STM and AFM to obtain the chemical data of our

surface. However, the resolution of Raman Spectroscopy alone is limited by the diffraction limit. And the intensity of the measurement signal[15]. Adding Tip-Enhanced Raman Spectroscopy(TERS) would allow us to bypass this diffraction limit get topographic chemical information of our sample at a molecular resolution, and significantly increase signal strength. The acquired data from TERS can then be combined with the topographical electronic structure simultaneously acquired using the STM component of the setup.

1.2 Scanning Tunneling Microscopy(STM)

Scanning Tunneling Microscopy, STM, first realized by Binnig and Rohrer[5] is a technique exploiting the phenomenon of quantum tunnelling to map the topography of surfaces.

Thus, to understand STM better, we will want to understand the phenomenon of Quantum Tunneling. To do this, we will look at a one-dimensional toy model.

1.2.1 Tunneling Current

To understand STM, we need to know how a particle that tunnels through a potential barrier behaves. The most relevant property we are interested in is its transmission coefficient. The probability that a particle goes through the potential barrier when it reaches it. We will inspect a barrier of relevance that can be characterized using equation 1.1. Which says there is a region in space, the interval $[a,b]$, where the system's potential energy is greater than the energy of the particle, E . Outside of this interval, the potential energy is less than that of the particle. The simplest version of this is for a constant $V(x) = \pm V$. Which is shown in figure 1.1, together with a gaussian and quadratic potential.

$$\begin{cases} V(x) > E & \text{for } a < x < b & (1.1) \\ V(x) < E & \text{for } x > b \text{ and } x < a & (1.2) \end{cases}$$

We will look at the solution from the Wentzel-Kramers-Brillouin(WKB) approximation.[18][31] From Sakurai, we learn that the idea behind this approximation is as follows: we assume that in the region of interest, the wavelength of the wavefunction is much shorter than the distance over

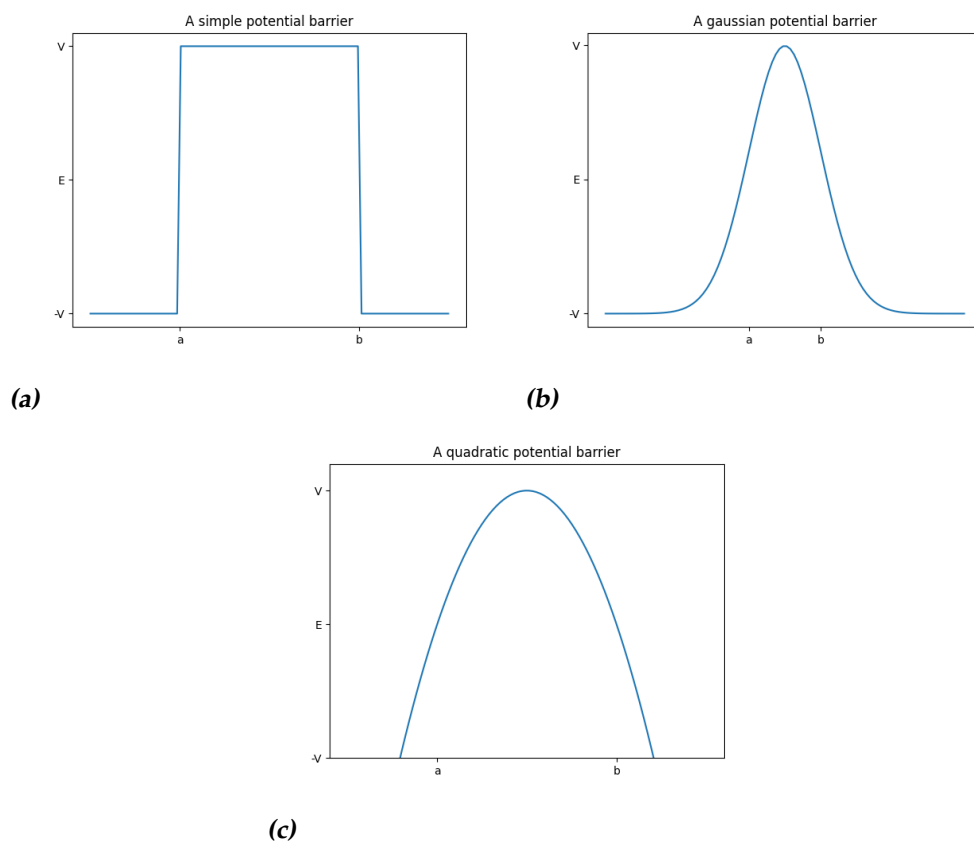


Figure 1.1: Several simple potential barriers for illustration.

which the potential energy varies.[31] This means that of our example potential barriers the approximation can not be applied to the square potential barrier because of its infinite steepness. But for potential barriers that our approximation can be applied to, the approximation gives the general transmission coefficient shown in equation 1.3 for our system. [31]

$$T \simeq \exp\left(-2 \int_a^b \sqrt{\frac{2m(V(x) - E)}{\hbar^2}}\right) \quad (1.3)$$

Here, a and b are the classical turning points, where $V(x) \approx E$. Thus, we integrate over the interval for which $V > E$.

We can learn from this solution that the transmission coefficient exponentially depends on an integral over the interval $[a, b]$. Then, because according to equation 1.1 $V(x) > E$ in this interval, the quantity inside of the integral has to be positive. Thus, as the interval $[a, b]$ grows, so does the solution of this integral.

This behaviour can be most easily seen by looking at an analytic solution for the square potential $V(x) = \pm V$ from Sakurai[31] and can be seen in equation 1.4.

$$T \simeq e^{-2 \frac{\sqrt{2m(V-E)}}{\hbar^2} (b-a)} \quad (1.4)$$

Here, the integral becomes a simple linear dependence on the distance $b - a$. It gives us an exponential dependence for our transmission coefficient. Thus, the qualitative behaviour of the tunnelling current is as follows: as the distance increases, the tunnelling current decreases exponentially.

1.2.2 Application to STM

Now, how does this relate to an STM? In an STM, you have an STM tip hovering above a conductive surface. The current wants to flow from the tip to the surface. But there is a potential barrier. This is the air or vacuum between the surface and the STM tip.

We have learned that this tunnelling current has an exponential decay, which can be leveraged when applying a feedback mechanism on the STM to perform topographic surface measurements.

The exponential decay of the tunnelling as the distance between tip and sample increases is also a property that helps enable the measurement of single atoms. The distance at which it decays is on the order of a magnitude per several Ångstrom. Or approximately the size of an atom. [10]

To conclude, the core property of an STM is that the measured tunnelling current decays exponentially as the distance between the STM tip and the surface increases.

1.3 Atomic Force Microscopy(AFM)

AFM was first realized by Binnig, Quate and Gerber. [4] It uses a tip mounted on a cantilever or quartz tuning fork to measure the tip surface interactions, which can be represented by a Lennard-Jones potential[24][26]. Similar to the tunnelling current in an STM, this can be used to create a topographic map of the surface using a feedback loop. [17]

This chapter will cover the theory behind Atomic Force microscopy to understand the design challenges behind adding AFM capabilities to the STM setup. To understand the challenges, we will first discuss the Lennard-Jones potential that AFMs measure and its regimes, followed by examining the mathematics of damped harmonic oscillators, which functions as a model of cantilevers and quartz tuning forks. Then, it will conclude by discussing the different excitation modes of the cantilever.

1.3.1 The Lennard Jones Potential

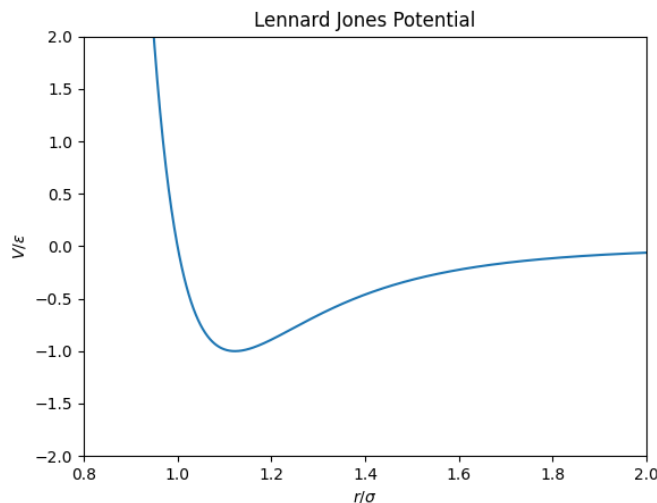


Figure 1.2: Here, we see the Lennard Jones potential plotted in dimensionless units. Here, ϵ is the potential well's dispersion energy or depth. σ is the distance at which the particle-particle interaction potential is zero. [24][26]

The Lennard-Jones potential is caused by an interplay between the repulsive electrostatic force and the attractive van der Waals force, and combined, they follow a Lennard-Jones potential. [24] [26] And can be empirically measured and verified using an AFM. This potential is given by equation 1.5 and shown in figure 1.2

$$V = 4\epsilon \left(\left(\frac{\sigma}{r} \right)^{12} - \left(\frac{\sigma}{r} \right)^6 \right) \quad (1.5)$$

Potential Regimes

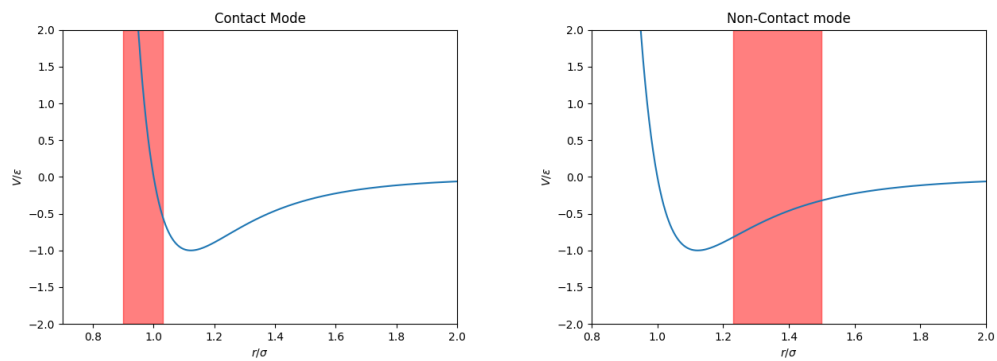
The Lennard-Jones potential we will measure is much more complex than the tunnelling current an STM measures. Because the force exerted on the AFM tip will be the gradient of the Lennard-Jones potential, where you measure along the curve will significantly influence the behaviour of the AFM tip. Thus, one can define three regions in the Lennard-Jones potential of different AFM tip behaviours highlighted in figure 1.3 based upon the slope of the curve.

This figure illustrates the three operational modes of AFM concerning the Lennard-Jones potential. The highlighted area is the potential range at which the AFM operates for the specific mode. 1.3a In contact mode, a large repulsive force acts on the tip and surface. This can be destructive to both the tip and surface. 1.3c: In tapping mode, the force applied to the AFM-tip oscillates between attractive and repulsive as the AFM-tip oscillates. This then leads to a tapping motion. This mode is less destructive to the surface than contact mode. 1.3b: In non-contact mode, a small attractive force exists between the AFM tip and the surface. Because of the distance from the surface, this force is relatively small compared to non-contact mode and does not oscillate between attractive and repulsive forces like tapping mode.[32]

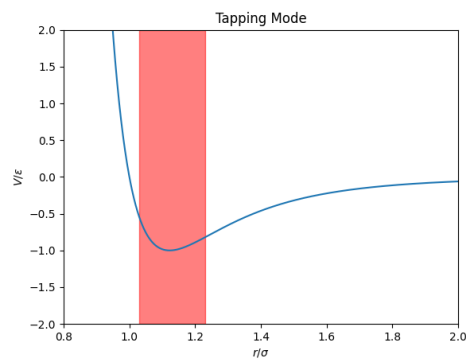
Different modes work better with different types of samples and set-ups. Thus, we must look deeper into the behaviour and effects of measuring in the different regimes to make better design decisions for our AFM.

For contact mode AFM, the biggest obstacle is the high forces applied to both the tip and the surface. These high forces can destroy the surface of the sample that is being measured. Thus, this type of measurement would not be appropriate for samples whose surface can easily be destroyed. [38]

On the other end of the spectrum is non-contact AFM. Here, the forces are much lower. This solves the main drawback of contact AFM. But this also poses several challenges. The force gradient will be lower with a range often lower than the size of condensation layers of water on top of



(a) A negative slope leading to a repulsive force. (b) A positive slope leading to a repulsive force.



(c) The global minimum of the potential, slight variations in position will change if you have an attractive or repulsive force

Figure 1.3: The three different potential regimes highlighted

the sample; the capillary force can then cause the AFM tip to get trapped in this layer and the cause the measured force to be the capillary forces instead of the surface-tip interaction.[23] Furthermore, it can cause the AFM tip to suddenly jump into contact mode if the Q-factor of the cantilever is too low. Thus, a cantilever with a high Q-factor, like a quartz tuning fork, is often preferred. [8] But as we later see, this causes it to become incompatible with AM-AFM.

The last of the three modes is tapping mode. This is a combination of both non-contact and contact AFM. In this mode, the cantilever will oscillate between contact and non-contact modes. Attempting to get the simplicity of setting up the measurement from contact mode but reduce its destructiveness by reducing the amount of time the AFM tip is in contact with the surface. Making it more useful for studying softer materials like biological samples or single-layer graphene.[32]

We now understand the possibilities of where in the potential we can measure. And the qualitative effect it will have on the cantilever. Now, let us look more closely at the equation of motion for an AFM cantilever.

1.3.2 The AFM Operation principle

In the original AFM by Binnig, Quate and Gerber[30], an oscillating cantilever was used. We ended up using a quartz tuning fork. But the mathematics behind the two are identical. Both systems are driven by damped harmonic oscillators that are governed by equation 1.6. Thus, understanding the damped harmonic oscillator will be essential to understanding the workings of AFM. And what qualities our AFM-resonator needs to possess.

$$\frac{d^2z}{dt^2} + \frac{\omega_0}{Q} \frac{dz}{dt} + \omega_0^2 z = \omega_0^2 A_{exc} \cos \omega t + \frac{\omega_0^2}{k} F_{ts}(z) \quad (1.6)$$

Here $\frac{\omega}{Q} \frac{dz}{dt}$ is the regular damping term caused by the air or fluid the oscillator oscillates in and the material the resonator is made of itself also has a finite damping. A_{exc} is the driving amplitude. F_{ts} the force between the tip and the sample, ω_0 is the resonance frequency, which is the driving frequency at which the oscillation of the resonator has maximum amplitude, k is the spring factor or stiffness of the cantilever and Q the quality factor.

Thus, we see that the oscillation of the resonator will depend on the force exerted by the surface onto the tip. And the variables we keep constant in a measurement will determine the exact solution.

But also, the properties of the resonator itself will influence the results. The resonance frequency will impact where we will measure, as discussed later, together with the stiffness and, most importantly, the quality factor.

For example, if the quality factor goes towards infinity, i.e., there is no energy loss in every oscillation, then we find that, as expected, our damping term tends to zero. We see this effect happen in measurements that occur in a vacuum. There, the quality factor of the oscillator increases for lack of air resistance, which this term models. However, a finite damping factor would remain from the inherent damping from the material the resonator is made of. This shows two ways the quality factor is influenced by the resonator. Damping from the air resistance will primarily come from the geometry of the resonator. And a leftover damping term is material dependent.

Thus, We will discuss the three main modes of driving the cantilever: Amplitude Modulation AFM, Frequency Modulation AFM and Phase Modulation AFM. These three modes each pick a different set of variables to keep constant and use as a feedback mechanism.

Amplitude Modulation AFM(AM-AFM)

In this mode, we start with a set driving amplitude and driving frequency around resonance. Our feedback variable here is the oscillation amplitude. We try to keep the system a constant ΔA away from a set oscillation amplitude by changing the height of the tip.

As the AFM tip scans the surface, the oscillation amplitude changes thanks to the forces between the surface and the tip from a change in resonance frequency. Thus, by applying feedback to keep the oscillation amplitude constant, one can measure the force gradient of the surface. [17]

The main advantage of AM-AFM is its electronic simplicity. But this comes at a cost when trying to reach higher-resolution measurements.

To understand this, we need to take a look at the minimum detectable frequency shift, $\delta(\Delta\omega)$ for AM-AFM. For as mentioned before the change in oscillation amplitude that we measure is from a change in resonance frequency. 1.7 [27][17]

$$\delta(\Delta\omega) = \sqrt{\frac{\omega_0 k_b T B}{2kQ\langle z_{osc}^2 \rangle}} \quad (1.7)$$

Here, B is the bandwidth, which can be considered a measure of the amount of pixels scanned per second, and $\langle z_{osc}^2 \rangle$ is the mean square amplitude of the cantilever's vibration. [17]

Here, we see that in AM-AFM, the resolution of our system increases as Q grows larger. Thus, if we were to only look at the signal-to-noise ratio, a higher Q cantilever is ideal, and it would also make an ideal candidate for vacuum-based AFMs. But we should also look at the transient time; this is the time it takes for our system to get to its steady-state solution after a perturbation. i.e., how long will it take for our measurement to be reliable as we move the cantilever from one spot to another? This transient time is given by equation 1.8.[1] [17]

$$\tau = \frac{Q}{\omega_0} \quad (1.8)$$

Here, we see that as Q increases, the time it takes for our system to reach a steady state after every measurement becomes longer and longer, making increasing the quality factor a double-edged sword and can make the measurement times unpractical.

The last important thing to mention for AM-AFM is its electronic simplicity, for our only interest is the oscillation's amplitude. [17]

We have learned that this technique works best where the AFM-resonator is either in liquid or air because of the quality factor constraints and its electronic simplicity.

Frequency Modulation AFM(FM-AFM)

In this mode, we start with a set variable and oscillation phase. The latter is set to 90 degrees, which is the value of the oscillation phase at resonance. The feedback variable here is the resonance frequency. We try to keep our system at a different frequency ω_{set} by changing the height of the AFM tip and then measure the difference between it and the resonance frequency $\Delta\omega = \omega_0 - \omega_{set}$. By keeping this constant using feedback, one can map the surface's force gradient.

The change in resonance frequency occurs from the difference in distance between the AFM tip and surface and, thus, in applied surface-tip forces. We use a phase-locked loop(PLL) to keep the oscillation phase at 90 degrees to stay at the resonance frequency.[7] If the oscillation amplitude is kept constant, one can disentangle the dissipative and conservative forces applied to the AFM tip. Which can not be done for AM- or PM-AFM.[17]

To understand the main advantage of FM-AFM, let us look at the minimum detectable frequency shift for FM-AFM, determined by equation 1.9 calculated by Albrecht et al.[1]

$$\delta(\Delta\omega) = \sqrt{\frac{2\omega_0 k_b T B}{k Q A^2}} \quad (1.9)$$

We note that the resolutions for FM and AM-AFM are similar. But in FM-AFM, the bandwidth is not dependent on the quality factor [1] [13][17] Thus, we do not have the problem we had for AM-AFM where the measurement speed slows down as Q increases, making it an ideal candidate for vacuum-based measurements.

This advantage, however, comes at the cost of using a PLL, increasing its electronic complexity and negating part of the advantage. [16]

We have learned that this technique has several advantages: greater resolution as Q increases the ability to distinguish conservative and dissipative forces and the ability to work in a vacuum. At the cost of electronic complexity. For our work, the greater the resolution as Q increases, and the ability to distinguish conservative and dissipative forces is the most relevant.

Phase Modulation AFM(PM-AFM)

We start with a set excitation amplitude and driving frequency in this mode. We set the latter at the resonance frequency far away from the surface. With our feedback variable being the oscillation phase, we try to keep our system a constant phase change, $\Delta\phi$, away from the phase at resonance by adjusting the AFM-tip height. [12] [16]

Without a feedback mechanism, the resonance frequency changes as we scan over the surface from a change in force. Which then changes the phase of our oscillation. If the surface is scanned, you will get a map of the phase gradient. [12] [16]

The main advantage of PM-AFM is that because of the lack of PLL usage, PM-AFM is electronically simpler. Allowing faster scanning. [16]

This scanning speed advantage comes at the disadvantage of being unable to distinguish between conservative and dissipative forces. And that the imaging range in height is limited for cantilevers with a high-quality factor [16]

Thus, we have learned that this technique is an excellent alternative to FM-AFM and AM-AFM if the priority is scan speed at the cost of height range and the ability to distinguish between conservative and dissipative forces.

1.4 Raman Spectroscopy

We have discussed how to get more topographical data. However, we are also interested in the molecular makeup of our system, with the long-term goal of identifying molecules attached to the edge of graphene.

For this, we use Raman Spectroscopy. With Raman spectroscopy, one aims a laser at a sample, which then scatters off the molecules in the same, causing the molecules to either start or stop vibrating. Making the laser light either lose or gain energy. This scattered light can then be measured, and one can use this to identify the molecule. [15]

1.4.1 The diatomic molecule

Now, let us first discuss Raman Spectra. We will talk about their origin through the lens of the diatomic molecule. For this, we will be drawing upon chapter 1.4 from Ferarro et al.[15]

Classically, one can look at a simple electromagnetic wave that fluctuates with time according to equation 1.10. In practice, this is the laser used to excite the Raman Spectroscopy sample.

$$E = E_0 \cos 2\pi\nu_0 t \quad (1.10)$$

Here, E_0 is the vibrational amplitude, and ν_0 is the laser frequency.

We then place a diatomic molecule in this electric field, which causes it to vibrate at a frequency ν_m . This molecule then generates an electric dipole, described by the polarization field from equation 1.11.

$$P = \alpha E = \alpha E_0 \cos 2\pi\nu_m t \quad (1.11)$$

This α is a proportionality constant. And is the key to Raman spectroscopy. α depends on the nuclear displacement. A larger nuclear displacement gives a larger nuclear dipole. The nuclear displacement is defined by equation 1.12. Here, x_1 and x_2 are the distance that each atom is away from its equilibrium position, illustrated in figure 1.4. In equilibrium, the nuclear displacement is, per definition, 0.

$$q = x_1 + x_2 \quad (1.12)$$

But how does the nuclear displacement change with time? It is a simple oscillation given by equation 1.13.

$$q = q_0 \cos 2\pi\nu_0 t \quad (1.13)$$

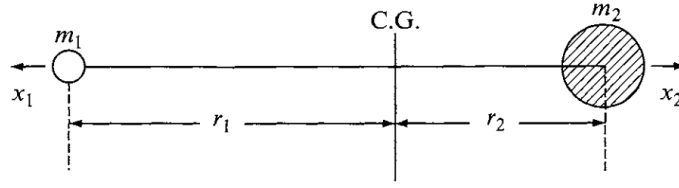


Figure 1.4: An illustration of the diatomic molecule. Here r_1 and r_2 is the distance of the respective atoms from the centre of gravity at equilibrium. x_1 and x_2 are the distance away from their equilibrium position, respectively, r_1 and r_2 . Image from Ferraro et al. [15]

Here q_0 is the vibrational amplitude. Now, let us assume that q_0 is small. Then let us make a Taylor expansion of $\alpha(q)$ around the equilibrium position, $q = 0$. This is then given by equation 1.14

$$\alpha = \alpha_0 + \left. \frac{\partial \alpha}{\partial q} \right|_{q=0} q + \mathcal{O}(q^2) \quad (1.14)$$

Here α_0 is α evaluated at the equilibrium position $q = 0$, thus $\alpha_0 = \alpha(q = 0)$.

Now, let us go back to the polarization field. If we combine equations 1.11 and 1.14 we are able to get the following equation 1.15

$$P = \alpha_0 E_0 \cos 2\pi\nu_0 t + \frac{1}{2} \left. \frac{\partial \alpha}{\partial q} \right|_{q=0} q_0 E_0 (\cos 2\pi(\nu_0 + \nu_m)t + \cos 2\pi(\nu_0 - \nu_m)t) \quad (1.15)$$

In the Polarization field, we see where Raman scattering comes from. The first term is the part of the light which gets scattered according to Rayleigh scattering. The 2nd and 3rd terms are anti-stokes and stokes scattering.

The other important thing we should read from this equation is that the Raman scattering terms both depend on $\left. \frac{\partial \alpha}{\partial q} \right|_{q=0}$. Thus, if $\left. \frac{\partial \alpha}{\partial q} \right|_{q=0} = 0$ then there is no Raman scattering. This means that the Polarization field can not be a local minimum or local maximum at $q = 0$.

Thus, we have learned that Raman scattering comes from the excitation of a molecule that exhibits stokes and anti-stokes scattering when the polarization field of the molecule has no local minimum or maximum at $q = 0$.

1.4.2 Tip-enhanced Raman Spectroscopy

Raman Spectroscopy has one major problem for us. Like other conventional optical methods, its resolution is limited by the diffraction limit and the signal intensity. [15][6][11][33] The method we want to use is called Tip-enhanced Raman Spectroscopy (TERS), first proposed by Wessel in 1985.[39] But it took until 2000 when the experimental technique was realized.[2][19][29][34]

To illustrate the physical mechanism behind TERS, we will cover the simple case of a single particle modeled as a homogenous dielectric sphere with Radius R that is smaller than the wavelength of a laser you are illuminating it with. This will show how the presence of a particle can cause the amplification of an electric field. This problem will simplify to the problem of a dielectric particle in a constant electric field as covered by Griffith's introduction to electrodynamics 4th edition chapter 4.[18] And illustrated in figure 1.5.

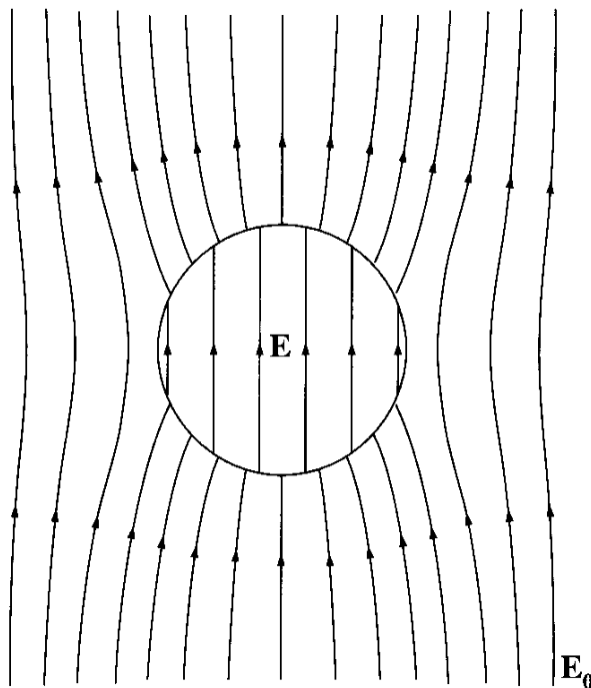


Figure 1.5: Here, we illustrate a small particle in an electric field. And how it perturbs a homogenous electric field in the \hat{z} direction. Taken from Introduction to Electrodynamics 4th edition chapter 4.4 by David J. Griffiths [18]

In our system, the only source of the electric or magnetic fields is the

laser. Thus we can use the quasi-static limit, i.e we assume we have no changing electric fields or magnetic fields. This means we must solve the Laplace equation for the electric potential. $\nabla^2 V = 0$

Our system has the boundary conditions as given by equations 1.16, 1.17 and 1.18 in spherical coordinates.

$$\begin{cases} V_{in} = V_{out} & \text{for } r = R & (1.16) \\ \epsilon_{in} \frac{\partial V_{in}}{\partial r} = \epsilon_{out} \frac{\partial V_{out}}{\partial r} & \text{for } r = R & (1.17) \\ \lim_{r \rightarrow \infty} V_{out} = E_0 r \cos(\theta) = E_0 z & & (1.18) \end{cases}$$

V_{in} is the electric potential inside of the dielectric sphere and V_{out} the electric potential outside. Through the method of separation of variables, one can get a general solution for the Laplace equation in terms of spherical coordinates given by equation 1.19 and equation 1.20.

$$V_{in} = \sum_{l=0}^{\infty} A_l r^l P_l(\cos \theta) \quad (1.19)$$

$$V_{out} = -E_0 r \cos(\theta) + \sum_{l=0}^{\infty} \frac{B_l}{r^{l+1}} P_l(\cos \theta) \quad (1.20)$$

Here $P_l(x)$ are the l th Legendre polynomials.

Using equations 1.16, 1.19 and 1.20, one can get a set of conditions for A_l and B_l as given by equations 1.21 and 1.22.

$$\begin{cases} A_l R^l = \frac{B_l}{R^{l+1}} & \text{for } l \neq 1 & (1.21) \end{cases}$$

$$\begin{cases} A_1 R = -E_0 R + \frac{B_1}{R^2} & \text{for } l = 1 & (1.22) \end{cases}$$

Then, one can do the same using the boundary conditions 1.17, which gives the system of equations given by equations 1.23 and 1.24.

$$\begin{cases} \epsilon_{in} l A_l R^{l-1} = -\epsilon_{out} \frac{(l+1) B_l}{R^{l+2}} & \text{for } l \neq 1 & (1.23) \end{cases}$$

$$\begin{cases} \frac{\epsilon_{in}}{\epsilon_{out}} A_1 = -E_0 - \frac{2B_1}{R^3} & \text{for } l = 1 & (1.24) \end{cases}$$

Then one can combine equations 1.21 1.22 1.23 and 1.24 which gives the expressions for A_l and B_l given by equations 1.25, 1.26 and 1.27

$$\begin{cases} A_l = B_l = 0 & \text{for } l \neq 1 & (1.25) \\ A_1 = -\frac{3}{\frac{\epsilon_{in}}{\epsilon_{out}} + 2} E_0 & \text{for } l = 1 & (1.26) \\ B_1 = \frac{\epsilon_{in} - \epsilon_{out}}{\epsilon_{in} + 2\epsilon_{out}} E_0 R^3 & \text{for } l = 1 & (1.27) \end{cases}$$

This allows one to find the expressions for \mathbf{E}_{in} and \mathbf{E}_{out} as given by equations 1.28 and 1.29.

$$\mathbf{E}_{in} = \frac{3}{\frac{\epsilon_{in}}{\epsilon_{out}} + 2} E_0 \hat{\mathbf{z}} \quad (1.28)$$

$$\mathbf{E}_{out} = \left(-E_0 - 2\frac{B_1}{r^3}\right) \cos \theta \hat{\mathbf{r}} - \left(-E_0 + \frac{B_1}{r^3}\right) \sin \theta \hat{\boldsymbol{\theta}} \quad (1.29)$$

Here $\hat{\mathbf{z}}$, $\hat{\mathbf{r}}$ and $\hat{\boldsymbol{\theta}}$ represent the unit vectors in the z , r , and θ directions. Note that we find that inside of the sphere the direction of the field is the same as the incident electric field. While the field outside of the sphere has a radial and polar component, hence why we stayh

If one then changes coordinate systems from spherical coordinates to cartesian coordinates for \mathbf{E}_{out} , one gets the expression given by equation 1.30.

$$\mathbf{E}_{out} = E_0 \hat{\mathbf{z}} - \alpha R^3 E_0 \left(\frac{1}{r^3} \hat{\mathbf{z}} - \frac{3z}{r^5} (x\hat{\mathbf{x}} + y\hat{\mathbf{y}} + z\hat{\mathbf{z}}) \right) \quad (1.30)$$

With $\alpha = \frac{\epsilon_{in} - \epsilon_{out}}{\epsilon_{in} + \epsilon_{out}}$.

Now, let us discuss what this result means. We notice that the resulting electric field outside the particle is a superposition of the electric field we originally applied and a dipole term.

This dipole term is what causes the interesting field configuration. When plotted, equation 1.30 gives figure 1.6. One then finds that the electric field is stronger near the small particle. This is the core principle behind TERS that is used to go past the diffraction limit. We note that in TERS, a metal tip is used and not a dielectric tip. But the field configuration will be similar.

Because we now know most of the signal is coming from the region of the enhanced electric field, the resolution is limited by the size of this region instead of the diffraction limit. This allows one, in theory, to measure smaller objects like molecules in this area that one can not see using conventional optical techniques.

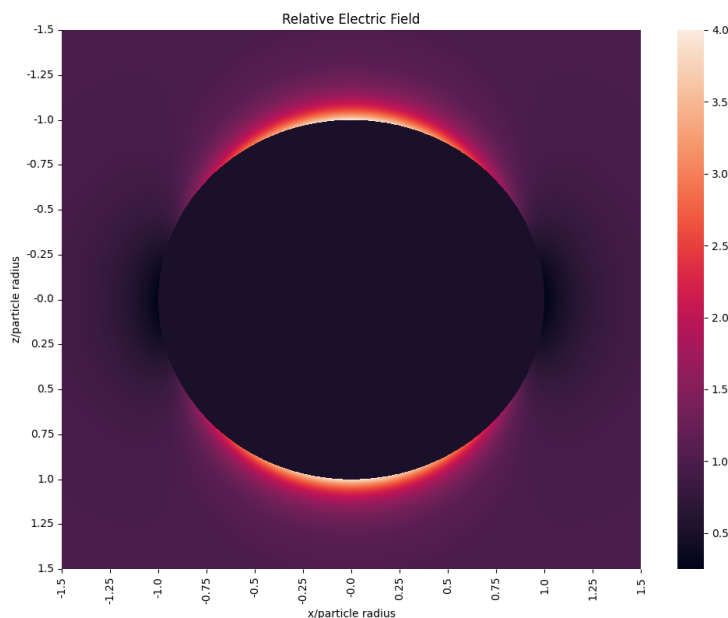


Figure 1.6: The relative electric field strength with respect to the applied electric field E_0 which was applied in the z direction. We note that along the z -axis just outside the particle, there is a significantly increased electric field strength. The increase in field strength from the laser light hitting these areas is the idea behind TERS. The Raman spectroscopy signal will be greatly enhanced if a molecule is in an area with enhanced electric field strength. Because the signal strength of Raman spectroscopy depends on E^4 [15]

This principle can then be applied in an STM. In the model, a small spherical particle was used, but the same effect can happen with an STM or AFM tip instead. Thus, by bringing an STM tip close to the surface on which you are performing Raman spectroscopy, the STM tip will act as an antenna. It amplifies the incoming unscattered laser light and the outgoing scattered laser light.

However, the amplification of the signal and resolution one can get is highly dependent on the shape of the tip, and not every tip will allow you to perform TERS. [21]

1.4.3 Comparing Raman Spectroscopy and Infrared spectroscopy

Now that we understand Raman spectra. Let us compare Raman spectroscopy to similar techniques like infrared (IR) spectroscopy. IR spectroscopy is based upon a similar principle. A laser makes the molecules vibrate, causing them to emit light. To better understand the differences, we will quickly discuss the physical differences between both methods and highlight two qualitative differences relevant to experiments.

The cause of the differences is that Raman and IR spectroscopy are based on different physical mechanisms. The mechanism for IR spectroscopy is based on changes in the molecule's dipole moment. And the absorption of light. [3], as we have seen for Raman spectroscopy, the mechanism relies on the change in the polarization, i.e. the dipole moment per volume and the scattering of light.[15] Because these two molecule properties exhibit different behaviours depending on the vibration, the IR active or Raman vibrations differ.

Rules have been devised based on the molecule's geometry to understand if a vibrational mode is Raman active, IR active or both Raman and IR active. These rules are derived from group and representation theory. For further reading on this, I suggest Ferarro et al.[15]

A practical difference between Raman and IR spectroscopy is the wavelengths one works at. As the name suggests, for IR spectroscopy, one works at infrared wavelengths, typically between $1 - 15\mu m$ [37] and typical Raman spectroscopy are in the visible light spectrum, $400 - 700nm$. [15]

Thus, we have seen that the main difference between Raman and IR spectroscopy comes from Raman Spectroscopy being based upon changes in the polarization. In contrast, IR spectroscopy is based on changes in the dipole moment. This has two main effects for experiments: a vibrational mode is often only Raman or IR active. And that Raman Spectroscopy works in a typical wavelength range of $400 - 700nm$ and IR spectroscopy in a range of $1 - 15\mu m$.

Instrumentation and Fabrication Methods

This section will discuss the instrumentation we used for Scanning Tunneling microscopy (STM) and Raman spectroscopy and the equipment we used to add AFM functionality to our STM.

2.1 STM Instrumentation

We use an in-house designed STM-head on which we place our measurement sample. We move the sample instead of the tip because our end goal is to do tip-enhanced Raman spectroscopy (TERS). There, we will have to focus a laser on the STM tip. If it were the tip that was moving, the laser would get out of focus from the tip as we scanned the surface.

For the electronics of our STM, we use a SoftDB MK2-A810 open-source SPM controller for the PID feedback.

In our system, we apply a voltage between the STM tip and the sample. Then, we proceed to measure the current that flows through the sample, which will be used as a feedback variable for our feedback loop.

A schematic overview of our STM setup and the feedback loop can be seen in figure 2.1

Because the current depends on the distance between the STM tip and the sample. We can keep the current constant by moving the sample's height as we scan its surface with the STM tip. By recording the z-offset, we can reconstruct the material's topographic surface.[10]

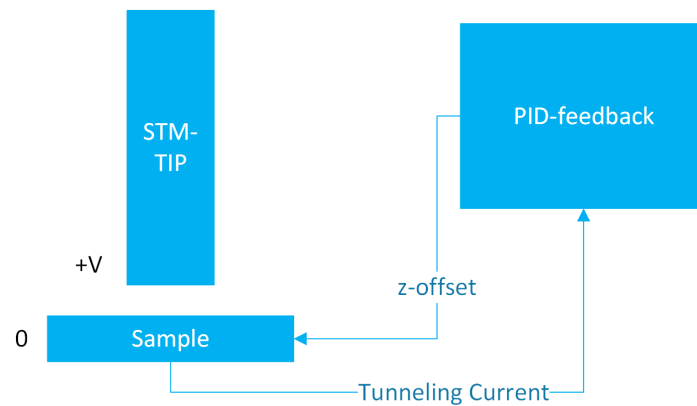


Figure 2.1: A schematic overview of the STM feedback loop.

2.2 AFM Instrumentation

We used a tuning fork onto which an STM/AFM tip was glued.

We use a phase-locked loop to keep the phase between the driving signal and the tuning fork constant.

To drive the AFM, we use the SoftDB MK3-PLL open-source SPM controller with PLL, and for the PID feedback, we use the SoftDB MK-2A810 open-source SPM controller.

A schematic overview can be seen in figure 2.2

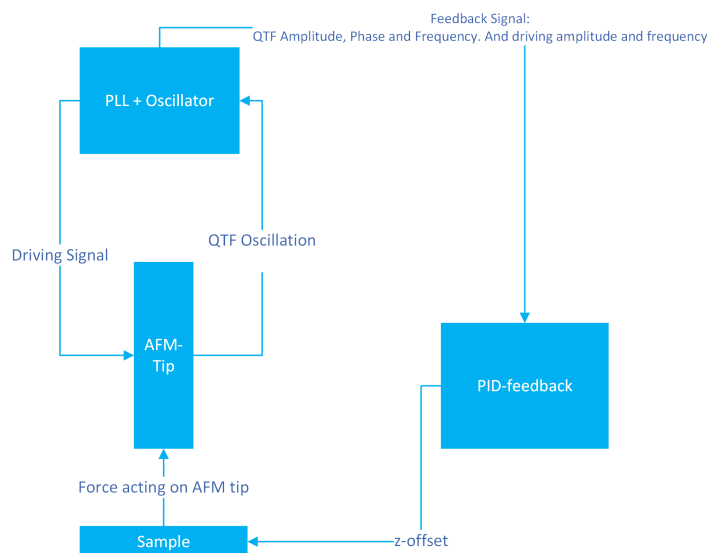


Figure 2.2: A schematic overview of the AFM feedback loop.

This system consists of two feedback loops. One is to control the height of the sample to keep the preferred property of our AFM tip on a Quartz Tuning Fork. This feedback loop is identical to the STM feedback loop illustrated in figure 2.1. A second feedback loop is applied onto the AFM tip that is placed upon a quartz tuning fork to drive its oscillation and control the mode in which we want our AFM to function, which uses the voltage from the QTF as an input signal.[17]

2.3 Raman Spectroscopy

For the Raman spectroscopy, we use a standard setup as shown in figure 2.3.

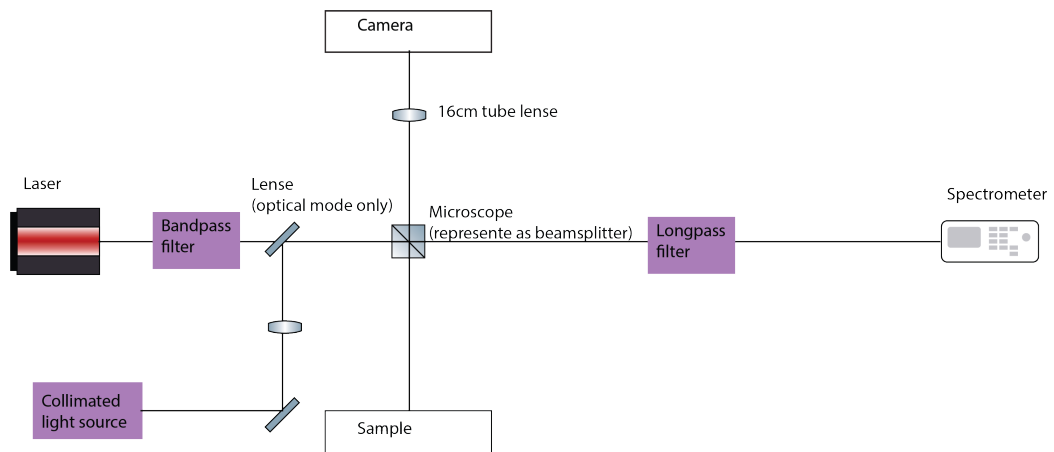


Figure 2.3: A schematic overview of the Raman Microscopy setup we used to take measurements. Here the laser light travels from the laser where the microscope focuses it onto the sample from where it goes towards the spectrometer.

For the laser, we use a diode-pumped solid-state laser (Lasos DPSS 523nm) with a wavelength of $\lambda = 532\text{nm}$. For the spectrometer, we use the Iso-Plane 160 from Princeton instruments with three gratings with the following sizes: 600 grooves per mm, 1200 grooves per mm and 1800 grooves per mm. A Thorlabs Mitutoyo apochromatic objective is used for the microscope at 10x and 50x magnification.

The bandpass filter is a 532nm high-performance laser line filter of 12.5mm diameter from Edmund Optics. Which removes the laser line harmonics that could otherwise cause noise.

The long pass filter is a 532nm laser line long pass filter of 12.5mm diameter from Edmund Optics. The long pass filter filters out laser light that gets reflected from the sample and does not interact with the measurement sample.

2.4 Fabrication of STM and AFM tips

We use nickel tips fabricated using Electrochemical etching for the STM and AFM.[22] [25] [9]

The basic process of electrochemical etching is straightforward. One puts a Nickel wire through a gold ring with a thin film of a 2M Potassium

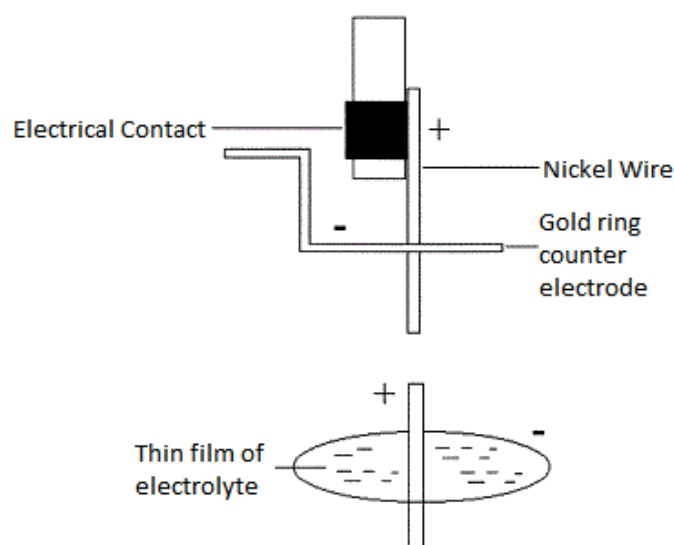


Figure 2.4: A schematic of our electrochemical etching setup to create our STM and AFM tips. The idea is to have a thin film of electrolytes in the gold ring. When we apply a negative voltage to the gold ring and a positive voltage to the nickel wire, the electrolyte starts corroding the nickel wire away. The lower figure is zoomed in on the gold ring. Figure modified from Kerfriden et al. [25]

Chloride(KCl) solution. Then, a voltage is applied between the gold ring and the nickel wire. See figure 2.4. This starts a redox reaction between the gold and KCl solution. For more details on the reaction, see Cavallini et al.[9]

The voltage we used varied between different setups to see if we could notice appreciable differences in tip quality. We varied from 1-4V in AC mode and a DC offset such that the voltage sign did not flip. We did not manage to draw any conclusions from varying the voltage. But an example STM tip is shown in figure 2.5

2.4.1 Sample Fabrication

Our measurements primarily used template-stripped gold to test our STM and AFM. This sample was fabricated by depositing a 100nm thick Au film on freshly cleaved mica using electron beam evaporation at approximately 300 degrees Celcius. Then, we attached a microscope glass coverslip piece to the top of the Au film using H70E epoxy from EpoTek. Removing the coverslip through force strips the Au film off the mica substrate, exposing an atomically flat surface with 50-100 nm-sized terraces.

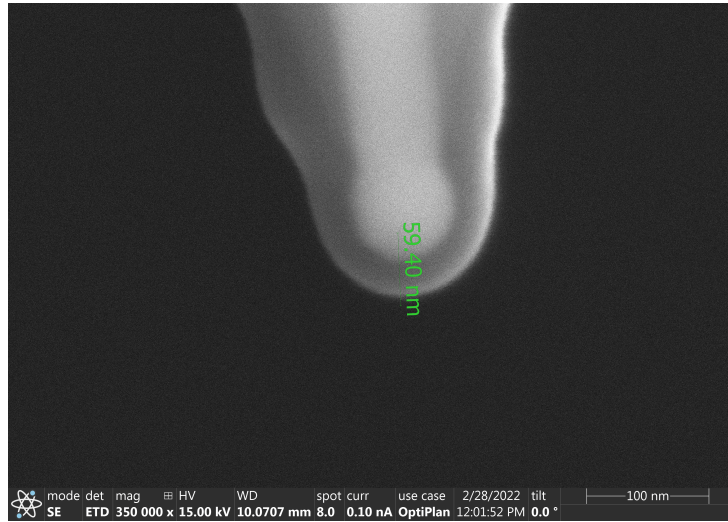


Figure 2.5: An SEM image of an electrochemically etched nickel STM tip. We note that the radius of curvature of the tip is approximately 60 nm.

We also performed measurements on HOPG. To prepare a HOPG sample, we would clean an already procured sample by exfoliating it using scotch tape.

Results and Discussion

In this chapter, we will discuss the results of our work. First, we will discuss the STM measurements we did to learn our setup at the start. We also did some simple noise analysis and discussed how we obtained measurements on HOPG. After that, we will discuss how we added AFM functionality to our STM and then show the measurements of the results. We will finish by showing some simple Raman spectroscopy results on graphene to understand our Raman spectroscopy setup and the effect of adding our combined STM/AFM setup to our Raman spectroscope.

3.1 STM Measurements on gold

We succeeded in measuring template-stripped gold on mica. Two measurements with the original setup are shown in the figures 3.1a and 3.1b. In figure 3.1b, we measured a terrace height of approximately $1\text{-}2\text{nm} \pm 1\text{nm}$. Which is similar to the 1.5nm value found by Hegner et al.[20]

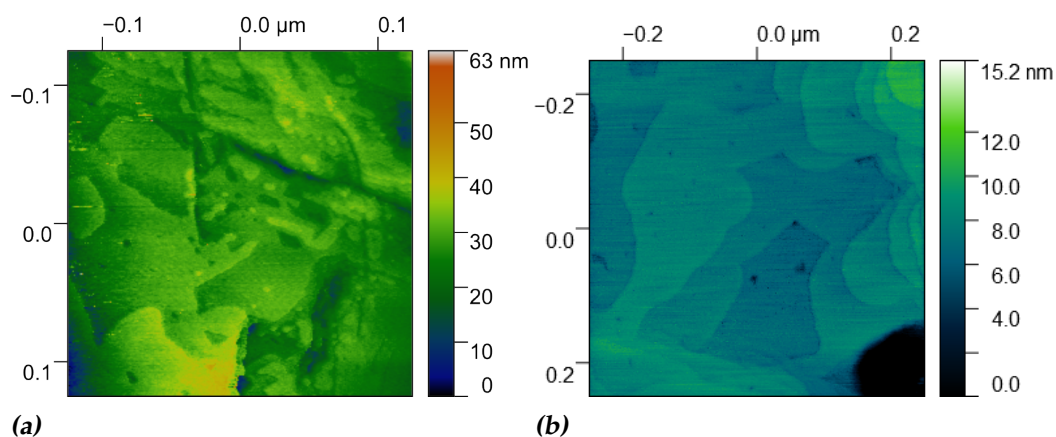


Figure 3.1: Two STM measurements we did of template stripped gold on mica. We note that the terrace height in figure 3.1a is $1-20 \pm 1 \text{ nm}$. Using the original STM setup. In figure 3.1b, the terrace height is more constant, approximately $1 \pm 0.5 \text{ nm}$. In both figure 3.1a and 3.1b, we notice features in the form of holes around $3-10 \pm 1 \text{ nm}$ wide.

3.2 Combining AFM and STM

We encountered several difficulties expanding the STM setup with AFM capabilities. Here, we will first go over setting up the AFM and the problems experienced during it. We will then discuss the measurements taken by the AFM.

Several challenges need to be solved to add AFM capabilities to an STM. The main challenges we encountered were deciding what type of AFM measurement, picking between a cantilever or a tuning fork-based AFM and then fabricating our chosen solution, figuring out how to get a tunnelling current from the AFM tip on the tuning fork, and combining the electronics leading to a final challenge of solving the physical geometry of the setup.

3.2.1 What type of AFM measurements?

The setup is being built with measuring molecules attached to the edge of graphene in mind. Graphene is very fragile. Thus, contact mode could destroy our sample. This would also be a problem for simultaneous AFM and STM measurements where contact AFM can cause the tunnelling current to grow too large. Thus, contact-mode AFM is preferably avoided, and tapping mode can also get dangerous because of the STM component.

Therefore, preferably, non-contact mode AFM would be used. But achieving tapping mode would already be a success.

For non-contact AFM, a high Q-factor is required, as discussed earlier. [8] We can thus disqualify using AM-AFM from our measurement, for it would become impractical thanks to increased measurement time as Q increases.

This leaves FM-AFM and PM-AFM. FM-AFM has the benefit of being able to separate dissipative and conservative forces by measuring the amplitude and frequency shift separately. [17] Compared to PM-AFM, the phase shift and amplitude shift both depend on the conservative and dissipative forces. [16] But PM-AFM is electronically simpler. And PM-AFM allows for faster scan speeds[16]. This would make FM-AMF preferable for making more qualitative measurements. But because of its electronic simplicity and scanning speed benefits, a PM-AFM mode would be a great boon.

3.2.2 Cantilever or Tuning Fork?

There are two common ways to do AFM: either you put a tip on a cantilever or onto a tuning fork. The main differences between these two are how to measure the deflection and their spring constant, resonance frequency, and quality factor. We will discuss these differences and then relate them to our measurement goals. Together with known theory, we can conclude whether a tuning fork or cantilever is superior.

The primary way to measure the deflection for the cantilever is by using a laser and detecting the reflected photons whose position will change as the cantilever oscillates. [17] The resonance frequency of cantilevers varies greatly and depends on the cantilever used. Its quality factor is often lower than that of a quartz tuning fork.

A tuning fork has a more straightforward way of measuring the deflection. As the quartz tuning fork vibrates, the piezoelectric effect causes an oscillation in voltage between the two forks of the tuning fork.[13] Allowing one to relate the voltage difference to deflection or to use it as a feedback variable. And has a relatively high-quality factor. Furthermore, it is relatively simple to fabricate in the lab for testing, as shown later

We require a high Q factor because we want to do non-contact AFM. This, together with the relatively simple manufacturing process of a quartz tuning fork with an AFM tip, makes using a tuning fork-based AFM ideal.

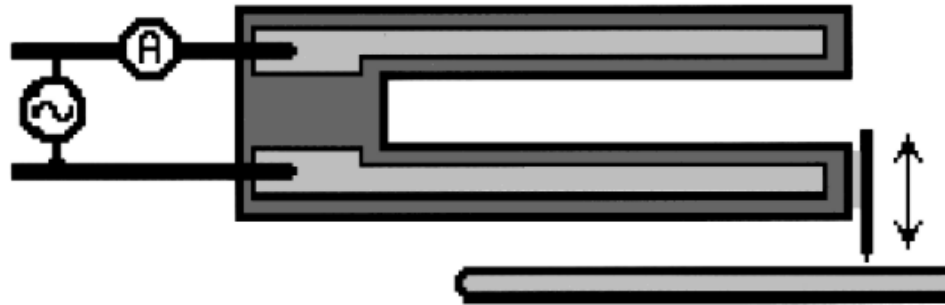


Figure 3.2: A tuning fork is used for AFM with an AFM tip attached to it and a circuit to measure the voltage between both forks of the tuning fork. Figure by Edwards et al. [13]

3.2.3 Fabrication of the Tuning Fork AFM tip

One of the most complex parts of setting up the STM/AFM was creating the tuning forks with an AFM/STM tip attached to the tuning fork, as shown in figure 3.2. The first step was creating a new STM/AFM tip using the previously discussed process.

Here, we encountered several challenges where, at its core, the main problem is the same. It is very simple to destroy the tip you are trying to attach, and you might not know until you have started attempting to measure. Or short-circuit the tuning fork when adding STM capabilities. But everything is straightforward. At first, we used non-conductive glue to attach the tip to the tuning fork and avoid short-circuiting. But we also wanted to attach a wire to the tip to apply a bias to the tip and do STM measurements while doing AFM simultaneously. This was done using conductive epoxy.

Attaching a wire to the AFM tips adds complexity. Because of the two separate glueing stages, this increased complexity makes it easier to destroy the tip and more time-intensive. One can also accidentally destroy this wire while putting the tuning fork into the STM/AFM setup. Do not use too much glue to avoid short-circuiting the tuning fork at this stage.

To combat this, we decided to go a different way to do combined STM/AFM by biasing the tuning fork. This allows us not to have to glue a wire to the STM/AFM tip separately. This causes the manufacturing process to be less error-prone.

We also found that the quality factor would significantly decrease when adding an AFM tip to the tuning fork. This could be mitigated by adding

another tip to the other side of the tuning fork to keep the mass of both forks of the tuning forks the same. This step is best done first to lower the chance of destroying the STM.

Understanding these properties was done by taking lots of frequency response curves. Figure 3.3 shows an example frequency response curve of an unmodified tuning fork.

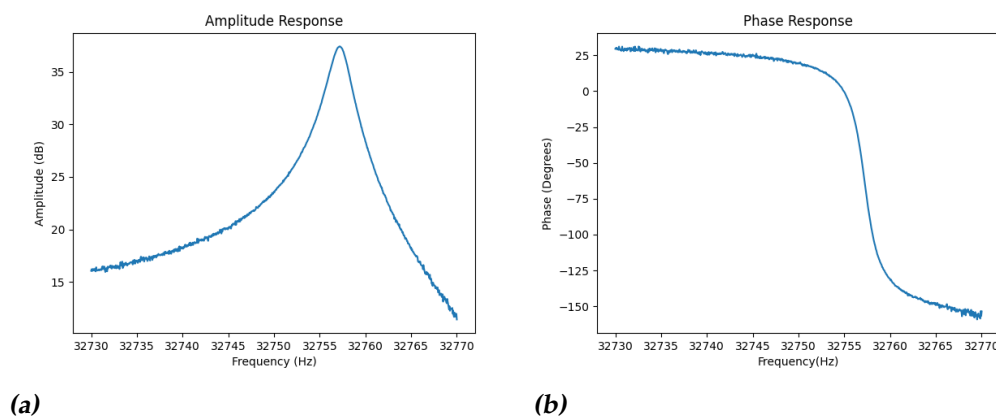


Figure 3.3: In figures 3.3a and 3.3b, we see the Amplitude and Phase-Frequency response curves of the tuning fork oscillation. This tuning fork has a resonance frequency of $f_{res} = 32757$ Hz and a quality factor of $Q = 13650$ as determined by the softDB-PLL software.

To summarize the manufacturing process, we followed the following process:

1. Manufacture a Ni STM/AFM tip
2. Take a frequency response curve of the tuning fork you plan to attach the tip to avoid having a broken tuning fork.
3. Attach STM/AFM tip to tuning fork using epoxy
4. Take a new frequency response curve to determine the quality factor and the resonance frequency.
5. Attach the tuning fork to the tip holder and put it into the STM/AFM.
6. Take a new frequency response curve to ensure the tuning fork was not damaged and to prepare for the measurements.

Now that we have discussed building our setup, we turn to the AFM results.

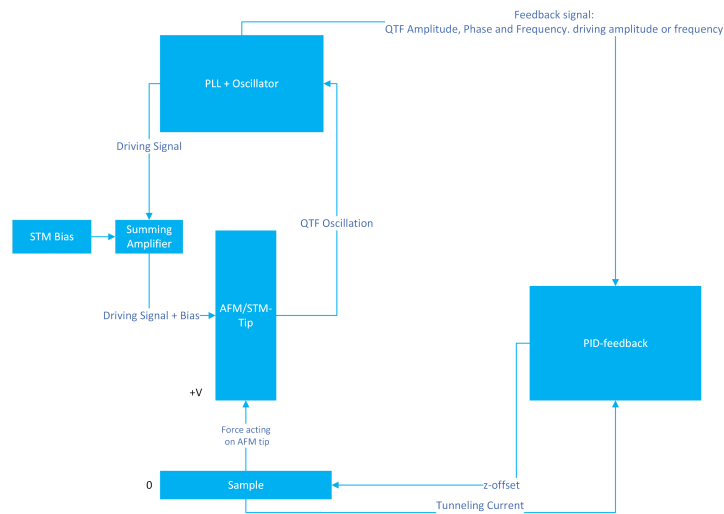


Figure 3.4: A schematic overview of the combined AFM plus STM setup.

3.3 AFM Measurements

Before an STM/AFM measurement can start, we must always measure our tuning fork's quality factor and resonance frequency first. This was done even if we reused a tuning fork after some time passed to ensure optimal conditions. We measured the quality factor and resonance frequency of the tuning fork by measuring the amplitude of the tuning fork at different driving frequencies.

We tested our AFM on the same gold samples we did STM on by doing simultaneous STM and AFM measurements.

Our best AFM-only measurement came during testing, where we measured a gold sample we had accidentally. This then showed weird round blobs on the surface of the gold. We think this is very likely dirt caused by touching it. This measurement is shown in figure 3.5. We know the sample was touched because we noticed a fingerprint on the sample.

Another test we did on several samples was taking frequency and phase distance curves. We set our AFM to FM-AFM mode. This gave us a characteristic Lennard-Jones-like potential for the frequency distance curves. An example measurement of a frequency distance curve is shown in figure 3.6.

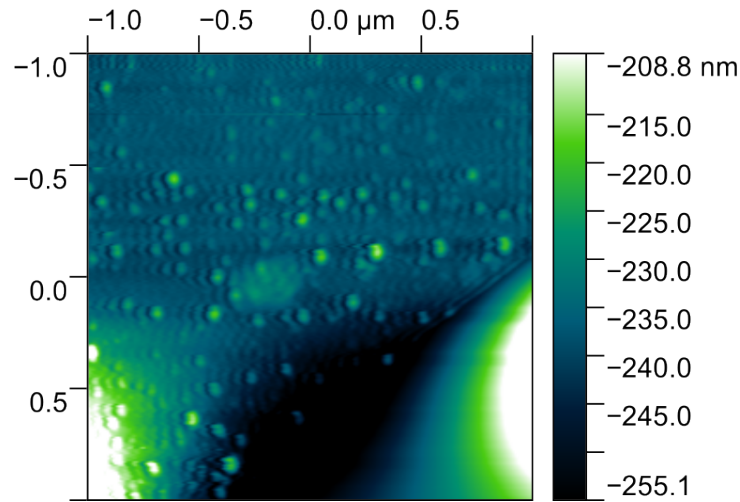


Figure 3.5: An early AFM we did of gold on mica. The weird blobs are hypothesized to be caused by a fingerprint left on the sample.

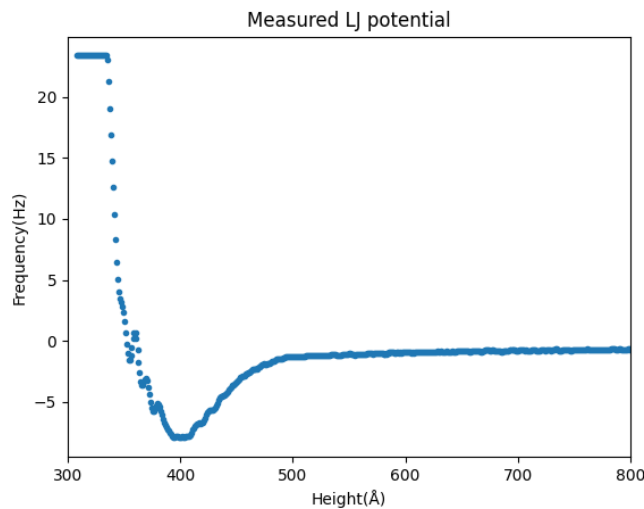


Figure 3.6: Here, we measure the frequency shift of the oscillation of the AFM tip with respect to the distance. On the x-axis is the reported slider extension attached to the AFM tip. The measurement was done by measuring the voltage generated by the tuning fork. After amplification, the voltage range was from -10V to +10V. Conversion of 428mV/Hz for this measurement leads to a range of -23.36 Hz to +23.36 Hz. We note that the graph resembles the shape of a Lennard Jones potential as expected. The graph flattens out at 23.36 Hz for the deviation exceeded the maximum frequency deviation for this measurement. The minimum of this measurement is at 392 \AA . The potential is zero at 350 \AA

3.4 Combining AFM and STM setups

After confirming that we could measure phase and frequency changes from our tuning fork, we needed a way to verify the validity of our AFM measurements. We decided to go to the next step and add back in STM capabilities. The main challenge we had to overcome was combining the STM and AFM's electrical circuits and keeping the manufacturing as simple as possible.

3.4.1 Tunneling Current

For manufacturing reasons, we decided to bias the whole tuning fork and not just the STM tip so that we could do STM measurements. But at this point, we still need to decide where to measure the tunnelling current. We decided to measure the current flowing from the sample side. For this was electronically the simplest. But adding a constant bias to the tuning fork has one more side-effect. It changes the equilibrium position of the tuning fork. This influences the measurements, and this change in equilibrium position would have to be corrected for force calculations. A schematic of the final setup of electronics and the feedback loop can be seen in figure 3.4.

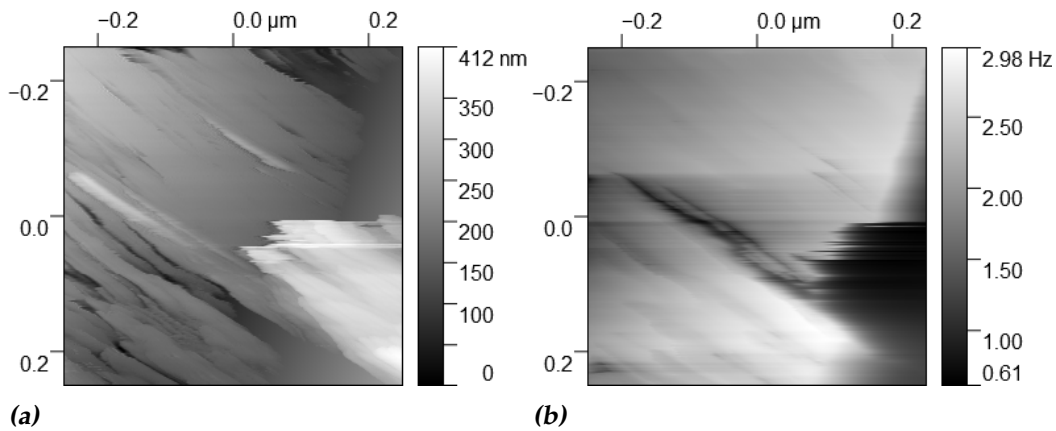


Figure 3.7: In figure 3.7a, you see an STM measurement done with the STM tip attached to the tuning fork. We operated the tuning fork in PM-AFM mode and captured the frequency shift in figure 3.7b as we tried to keep the phase constant.

3.5 Combined AFM/STM Measurements

After the STM and AFM setup were combined, we took STM measurements while driving the tuning fork and compared the frequency and phase to the topography we found from our STM measurements.

To do this, we found that the following steps worked best.

1. Approach the sample using the procedure for AFM.
2. Next, set the setpoint for the STM current to 0 to maximally retract.
3. When retracted, start driving the tuning fork.
4. Then, activate the feedback for the AFM or STM, depending on the measurement you want to perform.

Using this procedure, we took the measurements shown in figures 3.7 and 3.8.

In figure 3.7, we operated the tuning fork in PM-AFM mode by applying phase feedback through the PLL. However, the slider feedback was based on the STM. We found that this mode of operation for the tuning fork was the simplest to get working. You can see an apparent similarity between both measurements. However, we notice the STM measurement shows more unique features, of which not everything shows up in the frequency shifts measured.

Next, as you can see in figure 3.8, we did another STM measurement, but this time, we vibrated the tuning fork at a constant frequency and

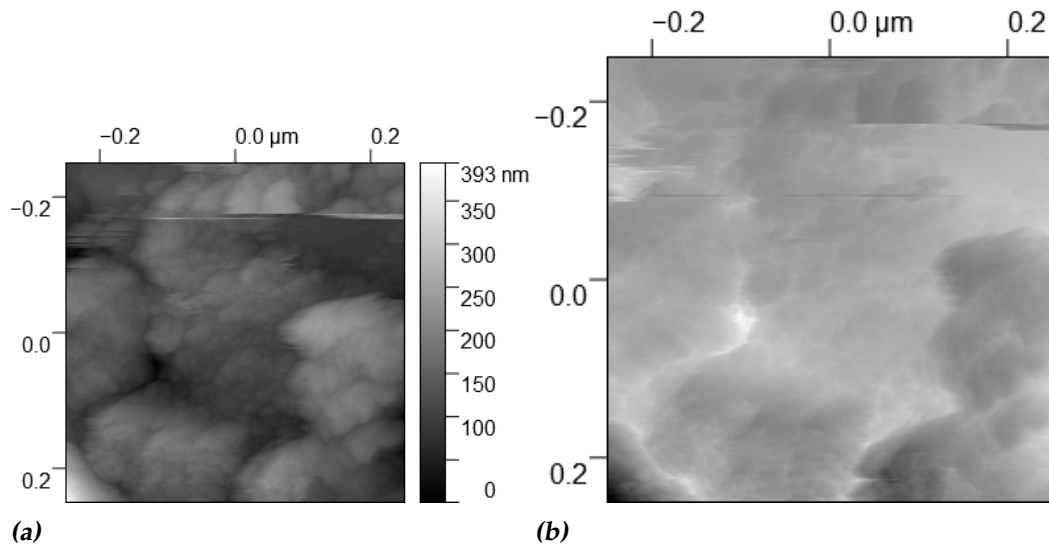


Figure 3.8: In figure 3.8a, you see an STM measurement done with the STM tip attached to the tuning fork. We operated the tuning fork at a constant frequency and captured the phase change as we scanned over the surface, as seen in figure 3.8b.

measured any phase shifts from the change in the tuning fork's resonance frequency. This set of measurements shows more apparent similarities.

Sadly enough, we could not get a simultaneous STM and AFM measurement with the tip of similar quality as has been done in earlier measurements, as shown in figure 3.1. We think this is because of the difficulties of setting up the AFM measurement and glueing the STM tip to a tuning fork, giving more opportunities to ruin the STM tip.

The measurement of dirt-like features on the touched gold sample, the frequency-distance curves and the simultaneous STM and AFM measurements where we encountered significant similarities between the STM measurement and the frequency and phase changes of our tuning fork, we ended up concluding that we successfully implemented AFM capabilities to our setup with the limiting factor being the quality of the AFM tip. This could relatively quickly be tested by buying a commercial AFM tuning fork and AFM tip and using it in our system. This would be a good next step for further exploring our setup's AFM and STM capabilities in the lab.

After we confirmed that the AFM/STM part of the system was functional in principle, we decided, for practical reasons, to move on towards putting the system under the Raman Microscope. At this point, we thought the main obstacle to a good AFM measurement was getting used to the manufacturing process and getting a good tip for AFM on a tuning fork.

Progressing towards simultaneous Raman spectroscopy and STM/AFM would be more important.

3.6 Combining STM/AFM with Raman Spectroscopy

The last system to integrate is the Raman spectroscopy setup. The main problem was fixing geometrical issues to get the three systems to fit together and operate simultaneously. This problem was twofold: making the structure of the STM/AFM fit with the Raman spectroscope and making the STM/AFM tip reachable by the laser light.

3.6.1 Geometry

When performing TERS, a laser will be focused on the STM tip. If we move the STM tip to scan a sample, we must also move the laser and keep it focused. To resolve this, we converted the system from moving the STM tip to moving the sample instead.

This, however, surfaced a new problem that was not apparent when the slider to move our sample was only moving an STM tip. A sample is much heavier than an STM tip. This caused the slider to move slower when bringing the sample up, closer to the tip, and faster when moving it down, away from the tip. This caused us to have trouble getting into tunnelling or AFM feedback.

This was partially caused by the spring attached to the slider. This would easily bend when changing the sample. The other cause was not found until after the end of the project. The problem was that only a single amplifier ran the STM slider's slip-stick motion. This amplifier was not strong enough to stop the slider from freefalling.

3.6.2 STM/AFM tip holder

We needed a tip holder so the microscope could focus on the STM/AFM tip. We have an in-house designed and built tip holder made for this. The latest version can be seen in figure 3.9

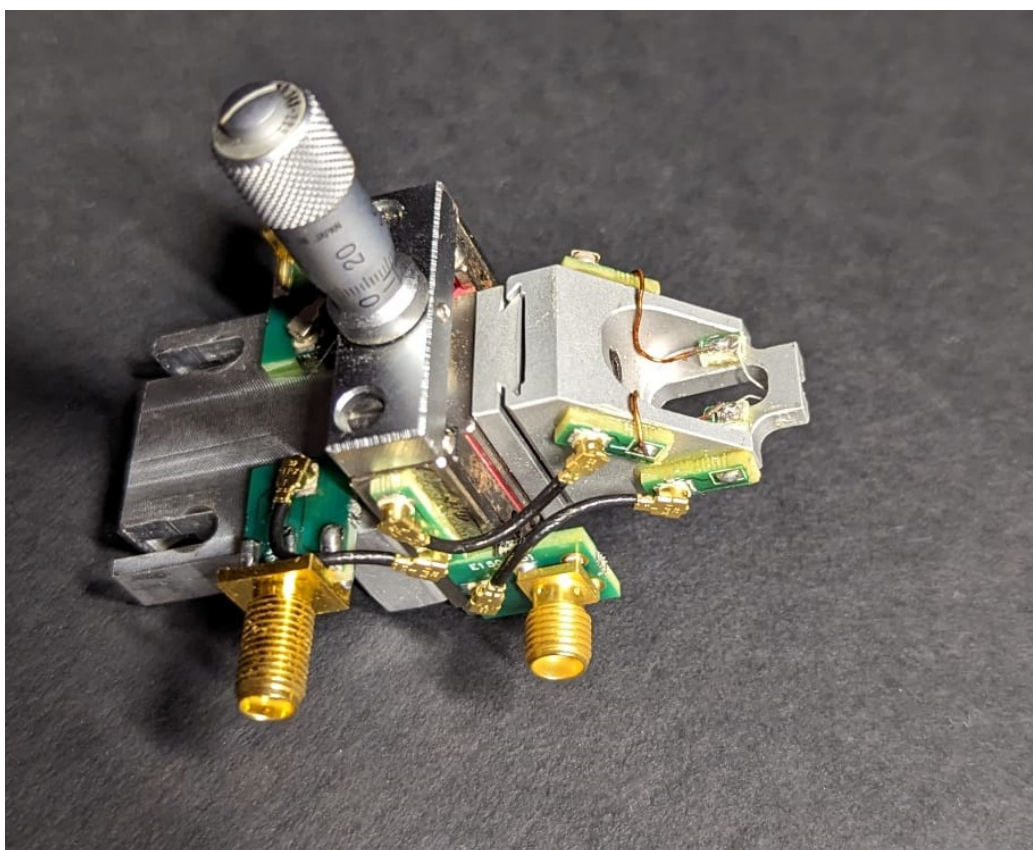


Figure 3.9: The latest tuning fork and STM tip holder.

3.7 Raman Spectroscopy Results

We succeeded in doing Raman spectroscopy measurements with a combined STM/AFM under the microscope. We managed to take a Raman spectrum of graphene on silicon oxide. However, we could only get the STM tip into tunnelling but not a good STM image of the graphene surface.

Figure 3.10 shows two example measurements of graphene on silicon. Together with an image of the laser for each respective measurement in figure 3.11. We note that the spectra we found are similar to those previously found in the literature.[14][28][36] From the G-band peak($k = 1600\text{cm}^{-1}$) being approximately half the size of the 2D-band peak($k = 2650\text{cm}^{-1}$). We can conclude that we were measuring single-layered graphene. Respectively, for multilayered graphene, the G-band peak would have been equal to or larger than the 2D-band peak. [36]

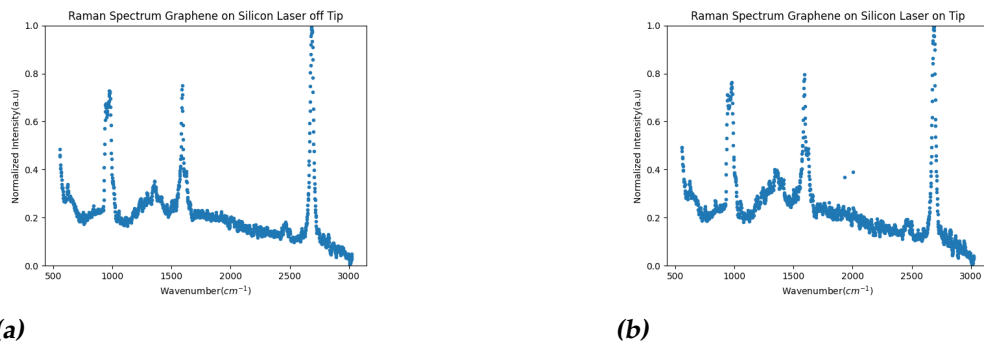


Figure 3.10: Two Raman spectra of graphene on silicon that we have taken. The minimum intensity of the spectrum was set as the 0 point, and the maximum intensity was normalized to 1. And the minimum In figure 3.10a, the laser was focused only on the sample and not the STM tip. In figure 3.10b, the laser is focused on both the tip and sample. The peak at 1000cm^{-1} and the one appearing at 500cm^{-1} was most likely caused by the silicon substrate. [35]

We also note that we could not get the laser as precisely focused on the sample and STM tip combined as we could when we were focusing on the sample. This is illustrated by figure 3.11. This did not seem to affect the Raman spectra we were taking except for a drop in total intensity.

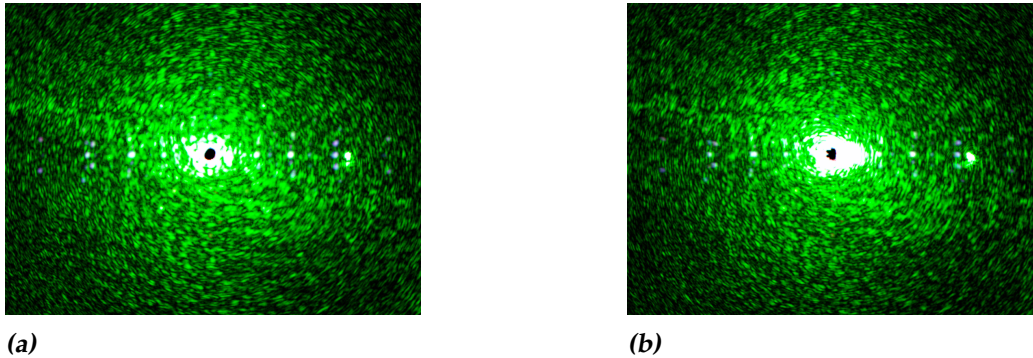


Figure 3.11: Two images of the laser is focused. In figure 3.11a, the laser was focused solely on the sample. And in figure 3.11b, the laser was focused on both sample and tip.

3.8 STM on HOPG under the Raman Microscope

To test the STM capabilities of our finalized setup, we first tested on more template-stripped gold. After which we proceeded to try and measure HOPG. Measuring HOPG was initially very difficult. We hypothesize that the problem was too flat of a surface for the STM tips we were measuring with. The measurements we managed to take were along a crack in the HOPG, and we managed to measure some terraces as seen in figure 3.12. The locations of these measurements are shown in figure 3.13. We think the area around this crack has a rougher surface. The terrace heights we measured ranged from 4 to $20 \pm 2nm$ at both spots.

In the STM measurements under the Raman microscope, we encountered a wavelike noise pattern towards the x-direction, with the wave having a period of $15nm$. But this noise seems filterable by applying a simple filter on the Fourier transform. As shown in figure 3.14.

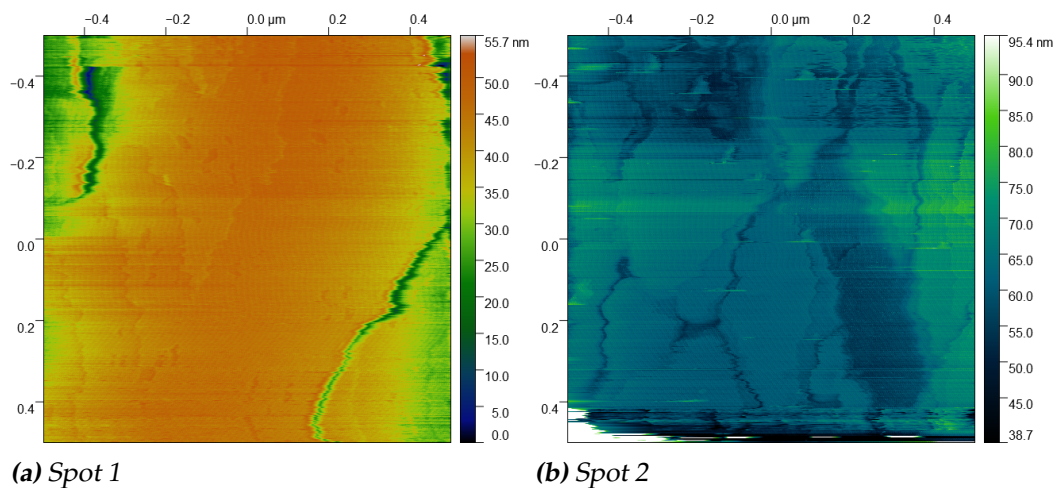


Figure 3.12: Two STM measurements of HOPG terraces. The location they were taken at is shown in figure 3.13.

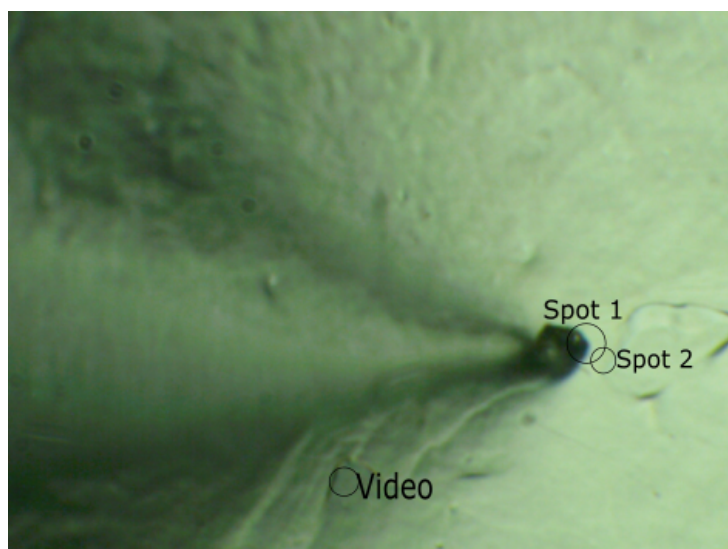


Figure 3.13: A map of measurement locations on Highly Oriented Pyrolytic Graphite (HOPG)

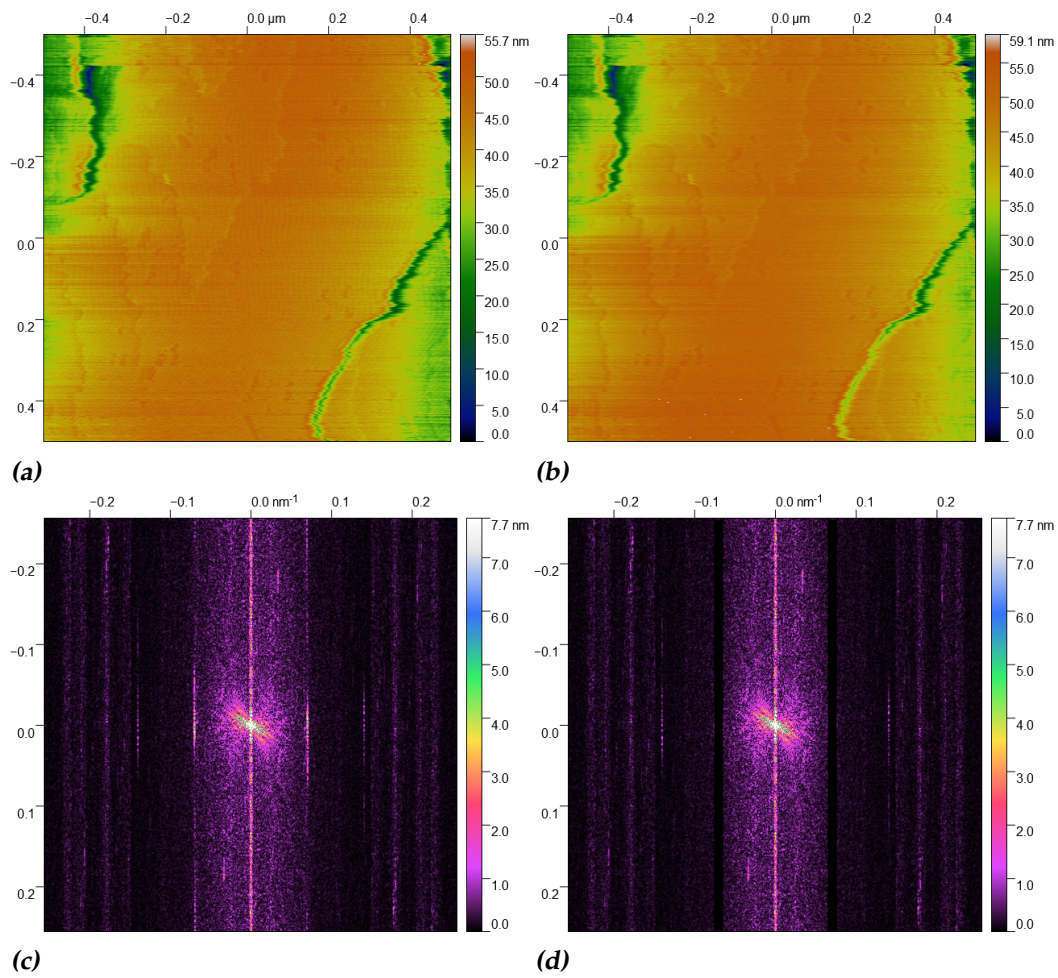


Figure 3.14: A before, figures 3.14a and 3.14c, and after, 3.14b and 3.14d, comparison of applying a simple Fast Fourier Transform (FFT) filter. The difference between figures 3.14a and 3.14b is shown in figure 3.15. This noise was only measured in one direction.

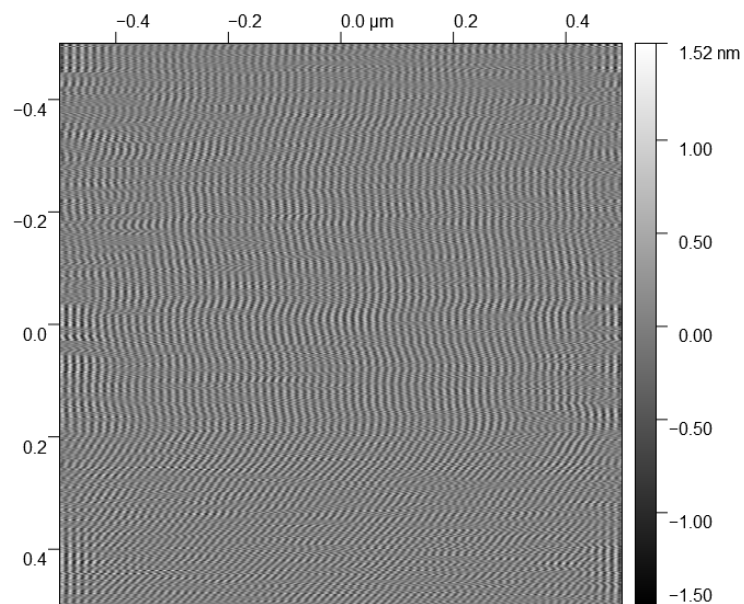


Figure 3.15: We subtracted figure 3.14b from 3.14a to illustrate the effect of the applied Fast Fourier Transform(FFT) filter

Chapter 4

Outlook

In this thesis, we have seen the setup of an AFM system, its combination with STM and its integration with a Raman microscope. In this chapter, we will discuss the future challenges left unresolved, our ideas on how to solve them and future applications of our system.

The unresolved challenges are as follows: First, improve the sensitivity and reliability of the AFM setup. Turning the AFM/STM + Raman scope into a TERS setup. And adding scanning Raman Microscopy to our Raman Microscope.

Let us start by discussing AFM sensitivity and reliability first. We think the system is fully capable of doing AFM measurements. To date, we have not been able to get measurements at a resolution that is satisfactory and close to that of our STM. We think the main problem holding us back is the AFM tip and tuning fork we have used. A way to test this would be to buy a commercial tuning fork-based AFM tip. Or improving the manufacturing of tuning forks with AFM tips and engineering tips specifically made for AFM instead of using Ni STM tips that we have been using up to now.

The next logical challenge for us will be getting a TERS signal. We have succeeded in focusing the laser beam on the STM tip and doing Raman Spectroscopy while the laser is focused on the STM tip. The next step would be to devise or replicate a simple experiment to check for a TERS signal. This would require a more quantitative understanding of TERS compared to the more qualitative understanding covered in our thesis.

The final remaining challenge is possibly the easiest. It enables scanning Raman spectroscopy. When integrating the STM/AFM with the Raman spectroscopy, we made it possible to move the sample using the STM/AFM system. Thus, this setup can now be used for scanning Ra-

man spectroscopy. This will require software integration with the Raman microscope software to perform measurements and either the STM/AFM control software or a custom-programmed solution. We suggest a combination of the two. Where the STM/AFM software is still used for movement. However, a script interfaces between the STM/AFM and Raman spectroscope software to do consecutive Raman measurements while scanning. This is such that once TERS capabilities have been achieved and simultaneous STM/AFM measurements are the next step, this can be taken care of by the already-used STM/AFM software.

Bibliography

- [1] Thomas R Albrecht, Peter Grütter, David Horne, and Daniel Rugar. Frequency modulation detection using high-q cantilevers for enhanced force microscope sensitivity. *Journal of applied physics*, 69(2):668–673, 1991.
- [2] Mark S Anderson. Locally enhanced raman spectroscopy with an atomic force microscope. *Applied Physics Letters*, 76(21):3130–3132, 2000.
- [3] David Warren Ball. *The basics of spectroscopy*, volume 49. Spie press, 2001.
- [4] Gerd Binnig, Calvin F Quate, and Ch Gerber. Atomic force microscope. *Physical review letters*, 56(9):930, 1986.
- [5] Gerd Binnig, Heinrich Rohrer, Ch Gerber, and Eddie Weibel. Tunneling through a controllable vacuum gap. *Applied Physics Letters*, 40(2):178–180, 1982.
- [6] E Blackie, EC Le Ru, M Meyer, M Timmer, B Burkett, P Northcote, and PG Etchegoin. Bi-analyte sers with isotopically edited dyes. *Physical Chemistry Chemical Physics*, 10(28):4147–4153, 2008.
- [7] Átila Madureira Bueno, José Manoel Balthazar, and José Roberto Castilho Piqueira. Phase-Locked Loop design applied to frequency-modulated atomic force microscope. *Communications in Nonlinear Science and Numerical Simulation*, 16(9):3835–3843, 2011.
- [8] Hans-Jürgen Butt, Brunero Cappella, and Michael Kappl. Force measurements with the atomic force microscope: Technique, interpretation and applications. *Surface science reports*, 59(1-6):1–152, 2005.

- [9] Massimiliano Cavallini and Fabio Biscarini. Electrochemically etched nickel tips for spin polarized scanning tunneling microscopy. *Review of scientific Instruments*, 71(12):4457–4460, 2000.
- [10] Julian Chen. *Introduction to Scanning Tunneling Microscopy Third Edition*, volume 69. Oxford University Press, USA, 2021.
- [11] Jon A Dieringer, Robert B Lettan, Karl A Scheidt, and Richard P Van Duyne. A frequency domain existence proof of single-molecule surface-enhanced raman spectroscopy. *Journal of the American Chemical Society*, 129(51):16249–16256, 2007.
- [12] U. Dürig, H. R. Steinauer, and N. Blanc. Dynamic force microscopy by means of the phase-controlled oscillator method. *Journal of Applied Physics*, 82(8):3641–3651, 1997.
- [13] Hal Edwards, Larry Taylor, Walter Duncan, and Allan J Melmed. Fast, high-resolution atomic force microscopy using a quartz tuning fork as actuator and sensor. *Journal of applied physics*, 82(3):980–984, 1997.
- [14] A. C. Ferrari, J. C. Meyer, V. Scardaci, C. Casiraghi, M. Lazzeri, F. Mauri, S. Piscanec, D. Jiang, K. S. Novoselov, S. Roth, and A. K. Geim. Raman spectrum of graphene and graphene layers. *Physical Review Letters*, 97(18):1–4, 2006.
- [15] John R Ferraro, Kazuo Nakamoto, and Chris W Brown. *Introductory Raman Spectroscopy*. 1994.
- [16] Takeshi Fukuma, Jason I. Kilpatrick, and Suzanne P. Jarvis. Phase modulation atomic force microscope with true atomic resolution. *Review of Scientific Instruments*, 77(12), 2006.
- [17] Ricardo García and Rubén Pérez. *Dynamic atomic force microscopy methods*, volume 47. 2002.
- [18] David J Griffiths. *Introduction to electrodynamics*, 2005.
- [19] Norihiko Hayazawa, Yasushi Inouye, Zouheir Sekkat, and Satoshi Kawata. Metallized tip amplification of near-field raman scattering. *Optics Communications*, 183(1-4):333–336, 2000.
- [20] Martin Hegner, Peter Wagner, and Giorgio Semenza. Ultralarge atomically flat template-stripped au surfaces for scanning probe microscopy. *Surface Science*, 291(1-2):39–46, 1993.

- [21] Teng Xiang Huang, Sheng Chao Huang, Mao Hua Li, Zhi Cong Zeng, Xiang Wang, and Bin Ren. Tip-enhanced Raman spectroscopy: Tip-related issues. *Analytical and Bioanalytical Chemistry*, 407(27):8177–8195, 2015.
- [22] Jhon P Ibe, Paul P Bey Jr, Susan L Brandow, Robert A Brizzolara, Nancy A Burnham, Daniel P DiLella, Kok P Lee, Christie RK Marrian, and Richard J Colton. On the electrochemical etching of tips for scanning tunneling microscopy. *Journal of Vacuum Science & Technology A: Vacuum, Surfaces, and Films*, 8(4):3570–3575, 1990.
- [23] Nader Jalili and Karthik Laxminarayana. A review of atomic force microscopy imaging systems: application to molecular metrology and biological sciences. *Mechatronics*, 14(8):907–945, 2004.
- [24] John Edward Jones. On the determination of molecular fields. -1. from the variation of the viscosity of a gas with temperature. *Proceedings of the Royal Society of London. Series A, Containing Papers of a Mathematical and Physical Character*, 106(738):441–462, 1924.
- [25] Sophie Kerfriden, Ayssar H NahlÃ©, Sheelagh A Campbell, Frank C Walsh, and James R Smith. Short communicationthe electrochemical etching of tungsten stm tips. *Electrochimica Acta*, 43(12):1939–1944, 1998.
- [26] John E Lennard-Jones. Cohesion. *Proceedings of the Physical Society (1926-1948)*, 43(5):461, 1931.
- [27] Yves Martin, Clayton C Williams, and H Kumar Wickramasinghe. Atomic force microscope–force mapping and profiling on a sub 100-Å scale. *Journal of applied Physics*, 61(10):4723–4729, 1987.
- [28] Zhenhua Ni, Yingying Wang, Ting Yu, and Zexiang Shen. Raman spectroscopy and imaging of graphene. *Nano Research*, 1(4):273–291, 2008.
- [29] Bruno Pettinger, Gennaro Picardi, Rolf Schuster, and Gerhard Ertl. Surface enhanced raman spectroscopy: towards single molecule spectroscopy. *Electrochemistry*, 68(12):942–949, 2000.
- [30] CF Quate and C Gerber. Atomic force microscope. *Phys. Rev. Lett*, 56:930, 1986.

- [31] J Sakurai and J Napolitano. Modern quantum mechanics. 2-nd edition. *Person New International edition*, 2014.
- [32] Alvaro San Paulo and Ricardo Garcia. Unifying theory of tapping-mode atomic-force microscopy. *Physical Review B*, 66(4):041406, 2002.
- [33] Feng Shao and Renato Zenobi. Tip-enhanced raman spectroscopy: principles, practice, and applications to nanospectroscopic imaging of 2d materials. *Analytical and bioanalytical chemistry*, 411(1):37–61, 2019.
- [34] Raoul M Stöckle, Yung Doug Suh, Volker Deckert, and Renato Zenobi. Nanoscale chemical analysis by tip-enhanced raman spectroscopy. *Chemical Physics Letters*, 318(1-3):131–136, 2000.
- [35] Paul A Temple and CE Hathaway. Multiphonon raman spectrum of silicon. *Physical Review B*, 7(8):3685, 1973.
- [36] Ying Ying Wang, Zhen Hua Ni, Ting Yu, Ze Xiang Shen, Hao Min Wang, Yi Hong Wu, Wei Chen, and Andrew Thye Shen Wee. Raman studies of monolayer graphene: The substrate effect. *Journal of Physical Chemistry C*, 112(29):10637–10640, 2008.
- [37] Randy L Wehling. Infrared spectroscopy. In *Food analysis*, pages 407–420. Springer, 2010.
- [38] Albercht L Weisenhorn, Mitra Khorsandi, Sandor Kasas, Vassilis Gtzos, and H-J Butt. Deformation and height anomaly of soft surfaces studied with an afm. *Nanotechnology*, 4(2):106, 1993.
- [39] John Wessel. Surface-enhanced optical microscopy. *JOSA B*, 2(9):1538–1541, 1985.